Model for core catcher ablation and cavity shape in the film regime

Alexandre Lecoanet, Michel Gradeck, Frederic Payot, Christophe Journeau, Nathalie Seiler, Nicolas Rimbert

Model for core catcher ablation and cavity shape in the film regime

A. Lecoanet[a,b,*], M. Gradeck[b], F. Payot[c], C. Journeau[a], N. Seiler[a], N. Rimbert[b]

[a] *CEA, DES, IRESNE, DTN, SMTA, Cadarache F-13108 Saint-Paul-Lez-Durance, France*
[b] *Université de Lorraine, CNRS, LEMTA, F-54000, Nancy, France*
[c] *CEA, DES, IRESNE, DER, Cadarache F-13108 Saint-Paul-Lez-Durance, France*

Abstract

During core meltdown in a nuclear reactor the corium may propagates toward the lower head and hit the vessel or structural elements as a coherent liquid jet. This could occur for instance in sodium fast reactors (SFR) if discharge tubes and an in-vessel core-catcher are used as mitigation devices. This can result in the ablation of the core-catcher and potential loss of its integrity. During ablation, a cavity is formed within the solid. Therefore the ablation of a solid structure by a liquid jet is studied here, with a focus on the cavity shape to improve future core-catcher designs. During the cavity formation, liquid flows over the cavity being formed as a liquid film in the film ablation regime, and ultimately results in the formation of a liquid pool. In the film ablation regime, two types of cavity shapes have been identified previously. To describe the process of the cavity formation, a mathematical model valid in this film ablation regime is here proposed which links the local melting rate to the local curvature of the cavity. It is applied with two sets of assumptions applicable to the two types of cavity previously identified. For the first assumption set, the heat transfer coefficient varies along the liquid/solid interface while the liquid temperature is held constant, it is representative of laminar boundary layer growth in laminar film. For the second assumption set, the heat transfer

*Corresponding author
Email address: alexandre.lecoanet@cea.fr (A. Lecoanet)

coefficient is held constant while the temperature varies along the liquid/solid interface, this is consistent with a turbulent liquid film. The two modeling approaches are compared with experimental data acquired from the HAnSoLO experimental setup. Numerical predictions show promising agreements with experimental observations, particularly for the laminar boundary layer growth zone of the cavity.

Keywords: Ablation, Core-catcher, Cavity shape, Melting, analytical model, Liquid jet

---

1. Nomenclature

Latin letters

B	Melting number	$\frac{C_{p,j}(T_j - T_{f,s})}{L + C_{p,s}(T_{f,s} - T_{0,s})}$	-
C_p	Specific heat	-	$J.kg^{-1}.K^{-1}$
D_j	Jet diameter	-	m
$\boldsymbol{e_r}$	Basis radial vector	-	-
$\boldsymbol{e_z}$	Basis vertical vector	-	-
F	Set representing the cavity	-	-
Fr	Froude number	$\frac{V_j}{\sqrt{gD_j}}$	-
g	Gravity acceleration	9.81	$m.s^{-2}$
h	Convective heat transfer coefficient	-	$W.m^{-2}.K^{-1}$
k_j	Thermal conductivity of the jet	-	$W.m^{-1}.K^{-1}$
L	Latent heat of fusion	-	$J.kg^{-1}$
$\mathcal{L}$	Curvilinear distance	Eq (7)	m
M	The point under consideration	-	-
$\dot{m}_f$	Surface mass flux	-	$kg.m^{-2}$
$\boldsymbol{N}$	Cavity normal vector at a given point M	-	-
Nu	Nusselt number	$\frac{hD_j}{k_j}$	-
Pr	Prandtl number	$\frac{\mu_j C_{p,j}}{k_j}$	-
Re	Reynolds number	$\frac{\rho_j V_j D_j}{\mu_j}$	-

r	Radial distance from jet axis	-	m
St	Stanton number	$\frac{h}{V_j \rho_j C_{p,j}} = \frac{Nu}{RePr}$	-
t	Time	-	s
T	Temperature	-	K
$\boldsymbol{T}$	Cavity tangent vector at a given point M	-	-
V	Average velocity along film thickness	-	$m.s^{-1}$
V_j	Jet velocity at impact	-	$m.s^{-1}$
V_f	Ablation velocity	-	$m.s^{-1}$
$\boldsymbol{x}$	Position vector	$\boldsymbol{x} = r\boldsymbol{e_r} + z\boldsymbol{e_z}$	m
z	Vertical coordinate	-	m
Greek letters			
α	Local cavity angle	-	^{o}
ΔT	Temperature difference	$T - T_{s,f}$	K
ε	Liquid film thickness	-	m
θ	Scaled temperature of the film	Eq. (25)	-
μ	Dynamic viscosity	-	$Pa.s$
ρ	Density	-	$kg.m^{-3}$
ϕ	Heat flux across liquid/solid interface	-	$W.m^{-2}$
Indices			
0	Initial		
f	Fusion		
j	Jet		
s	Solid		
$stag$	Stagnation zone		
Superscript			
$*$	Scaled variable		

2. Glossary

ASTRID	Advanced Sodium Technological Reactor for Industrial

	Demonstration
$BLG-1$	Refers to the first Boundary Layer Growth model defined by equation set (15)
$BLG-2$	Refers to the second Boundary Layer Growth model defined by equation set (16)
CTH	Refers to the Constant h model defined by equation set (30)
$ESFR-SMART$	European Sodium Fast Reactor - Safety Measures Assessment and Research Tools
$HAnSoLO$	Hot AblatioN of a SOlid by a Liquid – Observations
PWR	Pressurized Water Reactor
SFR	Sodium Fast Reactor

3. Introduction

During a severe nuclear accident a hot magma composed of both oxides from nuclear fuel and steel issued from reactor structure elements called corium may form. The corium may be relocated as a molten jet in the reactor lower part. The elevated corium temperatures (between 2 000 K and 3 100 K depending on its composition [1]) are likely sufficient to melt any steel structural elements of the reactor core with which it comes into contact (*i.e.* the corium ablates these structural elements).

In pressurized water reactors (PWR) jet ablation may occur during corium relocation toward the lower head [2]. The reactor vessel can therefore be weakened due to ablation from corium jets. Likewise, corium jets may form and interact with concrete of the containment if the reactor pressure vessel is breached [3]. Ablation of a solid structure by a liquid jet is therefore an important interaction in PWR safety studies [2]. Following the accident at Fukushima Daiichi, severe nuclear accidents with core meltdown must be mitigated from the early design phase of any new nuclear reactors [4].

This is especially true for the fourth generation of nuclear reactors that is

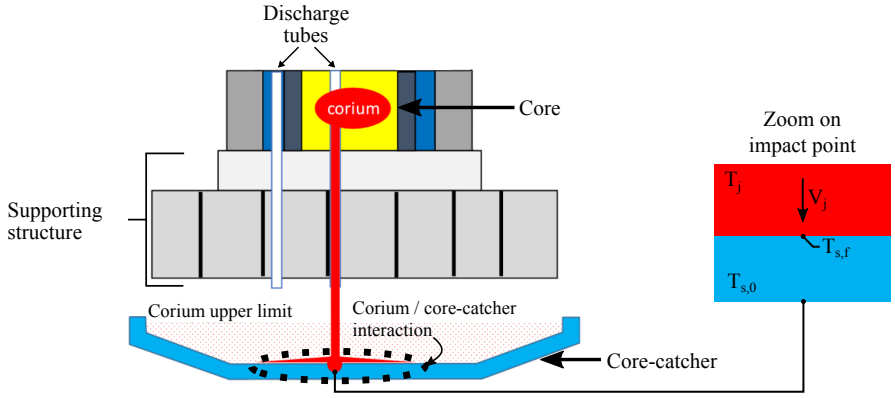

Figure 1: Schematic representation of corium relocation through discharge tubes to an SFR core-catcher. This system was chosen for the ASTRID project. Magnification of the jet impact point is presented with the relevant variables labeled.

currently under study and which must be even safer than previous generations [5]. Indeed, three of the eight goals of the Gen IV international forum relate to the safety and reliability of fourth generation reactors. The ablation of a solid structure by a liquid jet is of even greater relevance for sodium fast reactors (SFR), as it is rendered more likely by certain corium mitigation strategies. These mitigation strategies aim at relocating the corium as soon as possible onto a core-catcher placed inside the reactor vessel via discharge tubes in order to reduce the activity of the core region. The core-catcher purpose is to spread the corium so as to increase its coolability and avoid recriticallity. The ultimate goal is to stabilize the corium inside the reactor vessel. A Schematic of the discharge tubes/core-catcher system in a SFR is given in Figure 1. This corium relocation strategy was adopted for the ASTRID reactor design [1, 6, 7]. The present study aim to improve understanding of the ablation phenomenon that may occur during the relocation of the corium onto a core-catcher via the discharge tubes.

Corium may undergo phase segregation and a metallic phase as well as an oxide phase may coexist [8]. Depending on the accident progression, the corium jet may be composed of the oxides, or the metals or a mixture of both.

For SFRs, new reactor designs must consider how the impinged structure (*i.e.* the core-catcher) can be designed to withstand ablation, which requires understanding of the evolution of cavity shape. The present work aims to provide physical models for cavity shape estimation.

When a liquid jet enters a volume filled with liquid, heat is transferred more rapidly to its surrounding than when passing through gas. The jet may also more readily fragment prior to impact. Consequently, the thermal load of the jet on a solid surface is reduced if the jet passes liquid than if it passes through gas [9]. Furthermore, when the jet and the solid structure are of different nature or composition, the temperature of melting can be really different leading to a crust formation. This crust can be formed if melting temperature of solid is lower than the solidification temperature of the jet[1]. This crust could decrease the heat transfer and thus the ablation [10]. For severe accidents research, the worst case scenario for ablation must be considered. With what was just described this corresponds to the ablation of a solid by a liquid of the same nature as the solid passing through gas. For the core-catcher of an SFR this translates to the case of a metallic corium jet passing through a volume filled with sodium vapor, before impacting on a metallic core-catcher. This case is the focus of the present study. A completely dry lower head does not seems likely, however results obtained assuming a dry lower head give bounding values.

When a such liquid jet impacts a solid structure, it spreads over the surface and forms a liquid film. The heat transfer that ensues leads to very high heat fluxes, [11].

If the temperature of the jet is significantly higher than the melting point of the solid ablation occurs (*i.e.* the solid is drilled by phase change) and a cavity forms in the solid. During ablation, the liquid flow and the heat flux are strongly coupled, leading to complex heat and mass transfer phenomena.

[1] During the ablation of a steel structure by a corium jet composed of oxide a protective crust may form due to the difference between oxide solidus temperature $\approx$ 3 000 K and steel liquidus temperature $\approx$ 1 700 K.

In addition, as ablation proceeds, a cavity is formed and gravity may play a role, modifying the flow. Therefore, the cavity is the result of a highly coupled transport phenomena. The aim of this paper is to derive analytical models to predict the evolution of the shape of the cavity created by the ablation of a solid by a liquid jet.

During the course of ablation, two regimes, which occur sequentially, have been identified [10, 9, 12]. First, the liquid spreads over the solid as a film during the "film regime". Subsequently, when the cavity is deep enough, the film collapses and fills the cavity and the jet impacts on a liquid pool. This regime was first discovered by Saito *et al.* [10] and will be referred to herein as the "pool regime". For more details on pool regime, the reader is referred to [9] for phenomenological analysis and to [12] for a first analytic model describing the transition between these two regimes. This study focuses on the progression of the film regime.

The first theoretical study of ablation in the stagnation region of a jet was performed by Roberts [13]. This study dealt with submerged gas jets and was later expanded to liquid jets by Swedish *et al.* [14]. When both the jet and the solid are of the same composition, Swedish *et al.* [14] applied a method proposed by Epstein [15] to link the Nusselt number when melting of the solid occurs, Nu_f, to the one obtained when no melting occurs, Nu. The method employs a correction factor, given in equation (1), which makes use the melting number B, first introduced by Griffin [16].

$$Nu = \frac{B}{ln\,(1+B)} Nu_f \qquad with \qquad B = \frac{C_{p,j}\,(T_j - T_{f,s})}{L + C_{p,s}\,(T_{f,s} - T_{0,s})} \tag{1}$$

The theoretical study of Swedish *et al.* [14] (*i.e.* when the jet and the solid are not of the same composition and immiscible) was further experimentally validated by Furutani *et al.* [17]. Ablation velocity was investigated experimentally by [18, 10, 19] and more recently by [3]. These studies were focused on giving operational estimates for reactor design based on maximum heat transfer determined through the maximum ablation velocity, which was assumed to occur at the jet stagnation zone. To do so, Saito *et al.* [10] and Sato *et al.* [19]

carried out experiments where a liquid jet ablated a metallic plate. Sato *et al.* [19] focused on the case where the jet and the solid are of the same composition (tin on tin and stainless steel on stainless steel). The average ablation velocity was determined by recording the time needed to drill-through a metallic plate. From the ablation velocities, Sato *et al.* [19] obtained heat transfer data by assuming Newton's law, $\phi = h\,(T_j - T_{f,s})$, and using the Stefan condition with under-cooled solid. It led to equation (2) when the solid is of the same composition as the jet [19]. The relevant variables are given in Figure 1. In more details: V_f^0 is the ablation velocity along jet axis, $T_{s,f}$ is the melting temperature of the solid, $T_{s,0}$ is its initial temperature, L is its latent heat of fusion, $C_{p,s}$ is its specific heat, and ρ_s is its density. T_j is the temperature of the jet.

$$h\,(T_j - T_{f,s}) = V_f^0 \rho_s \left[L + C_{p,s}\,(T_{f,s} - T_{0,s})\right] \tag{2}$$

Saito *et al.* [10] and Sato *et al.* [19] thus obtained experimental values for h and proceeded to give experimental correlations linking the jet Nusselt number Nu, to the jet Reynolds number Re and Prandtl number Pr. These correlations only describe the heat transfer during ablation in the stagnation zone of the jet, where the heat transfer does not depend on the radial distance from the impact point [20]. In the present work the focus is on the cavity shape, related to the local heat transfer, and its evolution.

About the cavity shape, only Lipsett *et al.* [21] tried to model heat transfers outside the impact zone. They worked on a laminar impinging jet and focused on the situation where the distance between the nozzle and the solid is lower than one nozzle diameter. To solve the problem, the authors divided it into two issues; firstly, a potential flow and secondly, a boundary layer flow. The potential flow was solved using finite elements. It required an iterative process to obtain the gas/liquid interface which was part of the solution. The boundary layer flow was solved using integral boundary layer analysis. In comparison to Lipsett *et al.* [21] approach, this paper presents an analytical approach where the complete flow field is not solved and the location of the gas/liquid interface

is not sought. In the present piece of work, it is assumed that the jet is falling a long enough distance through gas (*i.e.* at least six jet diameters) so that the velocity field inside the jet can be considered as radially uniform [11].

More recently, in [12], it has experimentally been shown that cavity shape is time independent in film regime for jets with a constant temperature. Actually, the cavity grows in time by translating into the solid at a constant velocity. This indicates a quasi-steady state heat transfer at liquid/solid interface. In film ablation regime, the cavity shape is driven by heat transfer within the liquid film which itself is tightly related to the hydrodynamics of the liquid film. This means that the cavity shape is linked to the jet Reynolds number (Re). Two types of cavity shapes were identified [12]. Examples of these two types of cavities are available in Figure 2. For moderate Reynolds numbers ($Re < 66\ 500$, Figure 2a), the cavity can be divided into different zones as the curvilinear distance from impact increases: the first zone corresponds to the stagnation zone in which the cavity appears flat, in the downstream zone the boundary layer within the developing liquid film grows. Then transition to turbulence occurs and there the cavity appears flat again. Beyond this location, the film is fully turbulent up to the cavity end. For higher Reynolds numbers (Figure 2b), the boundary layer growth zone is not visible. At transition toward turbulence in the flowing film, the heat transfer to the solid increases. Likewise, the melting velocity increases and the depth of the cavity increases locally. However, because of back light illumination used in the experimental bench named HAnSoLO, a projection of the cavity shape is obtained. Therefore, the local increase in depth is not visible, and where it occurs, the cavity appears flat [9]. To summarize, in both cavity types, there is a stagnation zone, a boundary layer growth zone, a transition toward turbulence zone and a turbulent zone. But when the Reynolds number is high enough, the point where the melting velocity is the highest may not be the impact point. It may be located at transition toward turbulence instead. Therefore, breakthrough may occur outside of the jet impact point. In fact, the two types of cavity do not differ qualitatively but quantitatively.

In the scope of ESFR-SMART european project, under which the present

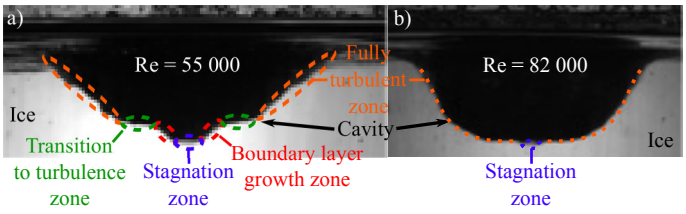

Figure 2: Examples of experimental cavity shape obtained with (a) $Re = 55\ 000$, where the stagnation zone, the boundary layer growth zone, the transition toward turbulence zone and the fully turbulent zone are visible, and (b) $Re = 82\ 000$, where the boundary layer growth zone is not visible [12].

study and the ones reported in [22, 9, 23, 12] were conducted, two prototypical experiments were conducted in KIT in the JIMEC facility [24, 25]. The results are still under analysis.

In the following, a model linking the local cavity angle to the local heat flux is presented. Then, this model is applied considering two sets of hypotheses. The first one is representative of the boundary layer zone visible in the first type of cavity described (*cf.* Figure 2a), and is referred to herein as the "BLG model", standing for Boundary Layer Growth model. It is assumed that liquid temperature stays constant outside the thermal boundary layer but the heat flux decreases radially as a consequence of an increase in heat transfer resistance[2] induced by an increase of the thermal boundary layer thickness. The second one is representative of a part of the second type of cavity described (*cf.* Figure 2b) in which the liquid film is mostly turbulent, and is referred to herein as the "CTH model", standing for ConstanT h model. It is assumed that heat transfer resistance is constant but that heat flux reduces radially because the liquid film temperature drops as it transfers heat to melt the solid.

It is the first time, to the best of authors' knowledge, that physical cavity shapes models are confronted to experimental data.

[2] An increase in heat transfer resistance is translated in Newton's law by a decrease in heat transfer coefficient.

4. Relation between the local cavity shape and the local heat flux

To model the cavity growth, a criterion must be obtained which links the cavity shape to local ablation kinetics. To do so, the following assumptions are made:

1. The cavity is axisymmetric;
2. The cavity shape is time independent [12];
3. The cavity grows into the solid by translating axially at constant velocity [9];
4. Melting makes the liquid/solid interface move along the normal to the interface on the local scale;
5. The maximum ablation velocity occurs in the stagnation zone[3];
6. Ablation velocity only asymptotically reaches 0.

A schematic description of the considered system is available in Figure 3. It is a cut of the cavity by a plane crossing its revolution axis. Jet impact point on the solid is noted as $O'(t)$ and algebraic condition $F(\boldsymbol{x}, t) = 0$ represents cavity points which will also be considered to be a member of the set F representing the cavity. The currently studied point is noted $M(\boldsymbol{x}, t)$ and, $\boldsymbol{x} = r\boldsymbol{e_r} + z\boldsymbol{e_z}$ where $\boldsymbol{e_z}$ and $\boldsymbol{e_r}$ are the vertical and the radial vectors of the cylindrical basis. The origin of radial distances is set on the jet axis. Vectors $\boldsymbol{N}$ and $\boldsymbol{T}$ are the normal and tangential vectors of F at point M. α is the angle between $\boldsymbol{e_z}$ and $\boldsymbol{N}$ (*cf.* Figure 3), which is also the local cavity angle. α gives the local evolution of the cavity height with the radial distance from impact point. It is therefore a measure of the local cavity shape. $\boldsymbol{V_f^0}$ and $\boldsymbol{V_f}$ are the ablation velocity at impact of the jet and at current point M respectively. As the cavity keeps its shape and translates along $\boldsymbol{V_f^0}$ direction, all points of F translate along $\boldsymbol{V_f^0}$, including M. However, melting at point M makes the cavity move along $\boldsymbol{N}$. Note that M is a coincident point and not a material point. M moves along

[3]This assumption leaves out the potential cases for which the maximum local ablation velocity may occur outside of the impact zone.

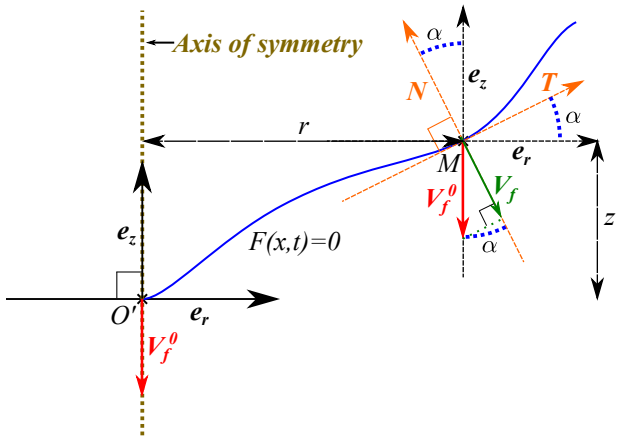

Figure 3: Schematic of the cavity indicating the velocities in equation (3).

the cavity to stay at a constant distance from impact point. Therefore, the projection of $\boldsymbol{V_f^0}$ onto the line $(M, \boldsymbol{N})$ is equal to $\boldsymbol{V_f}$. This leads to equation (3).

$$\alpha = \arccos\left(\frac{V_f}{V_f^0}\right) \tag{3}$$

Equation (3) shows that it is precisely the ratio between V_f^0 and V_f that is responsible for the curvature of the cavity F.

Note also that melting velocity may become infinitely small but never equates zero ($\alpha = \pi/2$ is only asymptotically reached). Equation (3) can be integrated to give the height of the cavity at a given radial distance r.

The derivative of z can be linked to angle α by equation (4). z' is consequently linked to $\boldsymbol{V_f^0}$ and $\boldsymbol{V_f}$ by means of equation (5).

$$z' = \frac{\mathrm{d}z}{\mathrm{d}r} = \tan(\alpha) = \frac{\boldsymbol{T}\cdot\boldsymbol{e_z}}{\boldsymbol{T}\cdot\boldsymbol{e_r}} \tag{4}$$

$$z' = \sqrt{\left(\frac{V_f^0}{V_f}\right)^2 - 1} \tag{5}$$

The evolution of z with r can be obtained by integrating equation (5). This

leads to equation (6).

$$z = \int_0^r \left[\sqrt{\left(\frac{V_f^0}{V_f\left(\mathcal{L}(0,r)\right)} \right)^2 - 1} \right] \mathrm{d}r \tag{6}$$

However, V_f depends on the curvilinear distance $\mathcal{L}(0,r)$ swept by the fluid between impact point O' and considered point M. This curvilinear distance is given by equation (7) and is itself a function of z'.

$$\mathcal{L}(0,r) = \int_0^r \left[\sqrt{1 + (z')^2} \right] \mathrm{d}\tau \tag{7}$$

5. Cavity and film models

The formulas derived in the latter section are applied to compute cavity shapes. Two limiting cases are investigated, based on two distinct sets of hypotheses defining two physical modeling approaches. Cavities produced by ablation in film regime are composed of four zones, the stagnation zone, the boundary layer growth zone, the transition toward turbulence zone, and the fully turbulent zone. The stagnation zone end point, here noted r_{stag}, was estimated by Stevens *et al.* [26] as:

$$\frac{r_{stag}}{D_j} = \frac{3}{4} \tag{8}$$

Also, depending on jet Reynolds number the extension of each of the three latter zones varies. For $Re < 66\,500$, [12], the boundary layer growth zone is clearly visible, Figure 2a cavity. The maximum cavity depth is located at jet impact point. When $Re > 66\,500$, [12], the transition toward turbulence and the fully turbulent zones prevail, Figure 2b cavity. Therefore, two models are proposed with assumption coherent regarding the boundary layer growth zone on one side and using assumption coherent with the fully turbulent zone on the other side. The boundary layer growth model (BLG) is relevant for $Re < 66\,500$ and results are validated on cavities obtained under this condition. The fully turbulent model, for which the heat transfer coefficient h is assumed constant

(CTH), is relevant for cavities obtained with $Re > 66\,500$, *i.e.* cavities for which the impact of the boundary layer growth zone on the cavity shape is negligible.

To determine the cavity shape according to equation (6), the ratio V_f^0 over V_f must be determined along the solid/liquid interface. To do so, the jump condition on enthalpy is used, equation (2). Equation (2) can be rewritten as equation (9) for an arbitrary temperature T and an arbitrary heat transfer coefficient h on the liquid side.

$$V_f = \frac{h\,(T - T_{s,f})}{\rho_s\,[L + C_{p,s}\,(T_{s,f} - T_{s,0})]} \tag{9}$$

The ratio V_f^0 over V_f can be written as equation (10), where 0 index refers to a quantity determined at impact point.

$$\frac{V_f^0}{V_f} = \frac{h_0\,(T_0 - T_{s,f})}{h\,(T - T_{s,f})} \tag{10}$$

In equation (10) two variables, h and T, may influence the ratio V_f^0/V_f which itself determine the local curvature of the cavity through equation (3). Therefore two limiting cases can be studied, namely the evolution of the cavity shape when the h varies while the T is held constant, and the evolution of the cavity shape when the T varies while the h is held constant. These limiting case correspond to the two models that are presented. The boundary layer growth model (BLG) is the one for which a constant liquid film temperature T is assumed, with a varying heat transfer coefficient h. BLG is representative of what occurs at the forefront of the cavity inside the boundary layer growth zone, before the transition toward turbulence. The constant h model (CTH) is the one for which a constant heat transfer coefficient h is assumed, with a variable liquid film temperature T. CTH is closer to what occurs when the liquid film is fully turbulent. Indeed, turbulence induces better mixing and a lesser dependence of heat transfer resistance to flow conditions.

5.1. Boundary layer growth models

In this section, laminar flow and boundary layer growth are considered. Schematic descriptions of both the cavity being ablated within the solid and the local system into consideration are available in Figure 4. On Figure 4a, the stagnation zone, where the thermal boundary layer is of constant thickness [20], is represented while the boundary layer growth zone is represented in Figure 4b. In the boundary layer growth zone, the surface temperature of the liquid film is expected to be constant, as experimentally proven by [12]. The temperature of the solid at solid/liquid interface is also constant. The heat flux between the solid and the liquid can be calculated using Newton's law, (*i.e.* $\phi = h\,(T - T_{s,f})$). The heat transfer coefficient h represents the effect of the thermal boundary layer on the heat transfer (linear approximation) and decreases as the thermal boundary layer grows. In this context, only h may vary in equation (10). Consequently in equation (6), the ratio of V_f^0 to V_f (respectively the melting velocity at impact, superscript 0, and at an arbitrary point of the cavity), is equal to the ratio of h_0 to h (with the same convention). As represented in Figure 4 the thermal boundary layer is of constant thickness [20] in the stagnation zone which means that h_0 is constant. Consequently, the local curvature of the cavity is 0, the cavity is flat, *cf.* equation (3). The heat transfer coefficient when melting occurs can be estimated from the one obtained when no melting occurs by means of the correction given in equation (1)[15, 9, 12]. The correction factor depends on the melting number B which in turns depends on the temperature and the properties of both the solid and the liquid which are, here, assumed constant. Consequently, the correction factors cancel out in the ratio of h_0 to h. This can be summarized by equation (11).

$$\frac{V_f^0}{V_f} = \frac{h_0}{h} = \frac{ln\,(1+B_0)}{B_0}\frac{B}{ln\,(1+B)}\frac{Nu_0}{Nu} = \frac{Nu_0}{Nu} \tag{11}$$

Finally, correlations proposed by [11] for heat transfer between a liquid jet and a flat surface without melting can be used for both the impact zone, *cf.* equation (12), and the boundary layer growth zone, *cf.* equation (13).

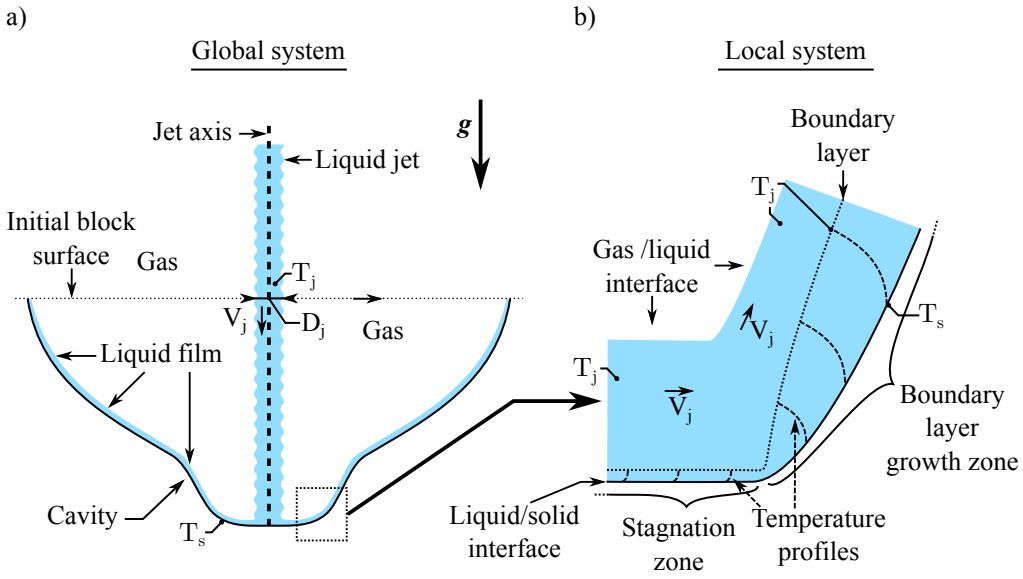

Figure 4: Schematic of (a) the global representation of the cavity ablated and (b) the representation of the transition between the stagnation zone, with a thermal boundary of constant thickness, and the boundary layer growth zone, within which the thermal boundary growth is observed.

$$Nu_0 = 0.745 Re^{\frac{1}{2}} Pr^{\frac{1}{3}} \tag{12}$$

$$Nu = 0.632 Re^{\frac{1}{2}} Pr^{\frac{1}{3}} \left(\frac{D_j}{r}\right)^{\frac{1}{2}} \tag{13}$$

In these equations, Nu, is the Nusselt number, Re is the jet Reynolds number, Pr is the jet Prandtl number, and D_j, ρ_j, μ_j, k_j and $C_{p,j}$ are respectively the diameter, the density, the dynamic viscosity, the thermal conductivity and the specific heat of the jet. The cavity shape can therefore be computed with equation (6) using:

$$\frac{V_f^0}{V_f} = \frac{Nu_0}{Nu} = G\sqrt{r} \qquad ; \qquad G \approx \frac{1}{0.848 \cdot \sqrt{D_j}} = \frac{1.179}{\sqrt{D_j}} \tag{14}$$

As a first approximation, the curvilinear distance of a given point M from impact point O' can be identified to its radial coordinate r, *i.e.* $\mathcal{L}(0,r) \approx r$. Moreover, heat flux is constant from impact point to the end of the stagnation zone [20], cf. equation (8). So the cavity is flat in the stagnation zone. With these approximations, evolution of the cavity height with r is thus given by the following set of equations (15), which define the BLG-1 model.

$$\boxed{z = \begin{cases} 0 & : \quad r \leqslant r_{stag} \\ 0.48 \cdot D_j \left(\frac{1.39}{D_j} r - 1\right)^{3/2} & : \quad r > r_{stag} \end{cases}} \tag{15}$$

More rigorously, one can replace the radial distance by the actual curvilinear distance from the impact point by combining equations (5), (7) and (14). The evolution of the cavity height with the actual distance from the impact point is thus given by the following set of equations (16), which define the BLG-2 model.

$$\boxed{z = \begin{cases} 0 & : \quad r \leqslant r_{stag} \\ \displaystyle\int_{r_s}^{r} \sqrt{G^2 \left(\sqrt{r_{stag}} + \frac{G}{2}\left(r - r_{stag}\right)\right)^2 - 1}\ \mathrm{d}r & : \quad r > r_{stag} \end{cases}} \tag{16}$$

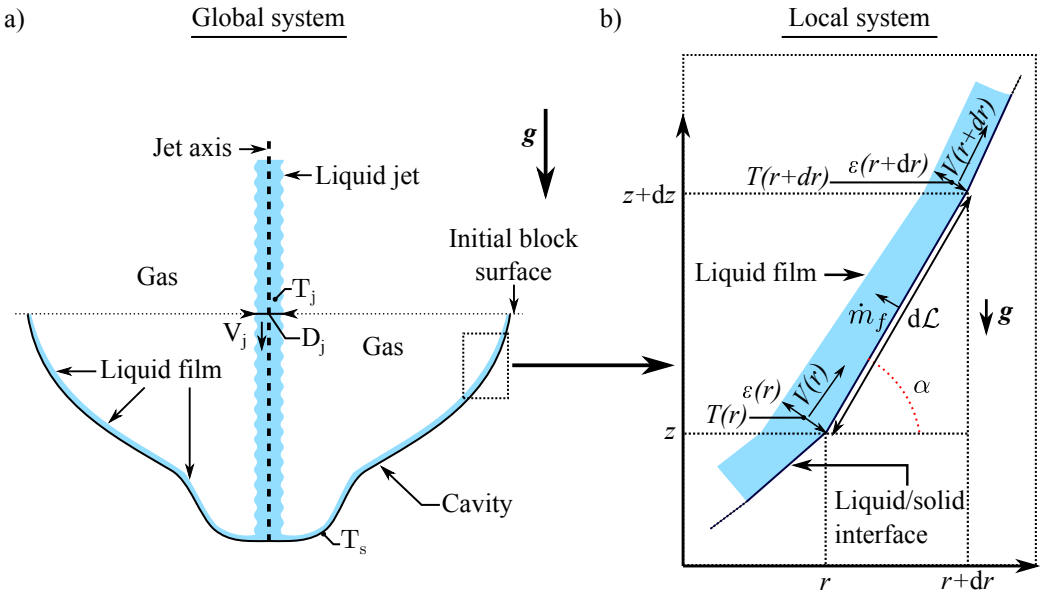

Figure 5: Schematics of (a) the global physical system under consideration and (b) the local physical system considered to establish the CTH model presented in section 5.2, *cf.* equation (30).

5.2. Constant h model

The global physical system under study is shown in Figure 5a while the local physical system is given in Figure 5b. The relevant parameters, are reported on Figure 5. In the present section, it is considered that the heat transfer coefficient h is constant, while the average temperature of the liquid film T varies. It is assumed that the liquid film is well mixed throughout the film thickness leading to a uniform temperature of the liquid film perpendicularly to the liquid/solid interface. The change in heat transfer along the cavity thus stems from the change in the liquid temperature T. As the heat is absorbed from the liquid phase by melting of the solid, T decreases. An analytical model is thus derived for the liquid temperature evolution.

The analysis is carried out on the differential system displayed Figure 5b. ε is the film thickness, V is the average velocity along film thickness, and $\dot{m}_f$ is the

mass flux of liquid produced by melting[4]. Equation (17) gives the liquid/solid boundary elementary surface.

$$\mathrm{d}S = 2\pi r \mathrm{d}\mathcal{L} \tag{17}$$

Using equation (17), a mass balance is derived, equation (18). Making dr infinitely small and using equation (19) gives equation (20).

$$2\pi\rho r\varepsilon(r)V(r) + 2\pi r\dot{m}_f \mathrm{d}\mathcal{L} = 2\pi(r+\mathrm{d}r)\rho\varepsilon(r+\mathrm{d}r)V(r+\mathrm{d}r) \tag{18}$$

$$\frac{\mathrm{d}\mathcal{L}}{\mathrm{d}r} = \frac{1}{\cos(\alpha)} \tag{19}$$

$$\frac{\dot{m}_f}{\cos(\alpha)} = \frac{\mathrm{d}\left(\rho\varepsilon V\right)}{\mathrm{d}r} + \frac{\rho\varepsilon V}{r} \tag{20}$$

Likewise, heat balance gives equation (21). Going to the limit $dr \to 0$ and using equation (19), equation (22) is obtained, in which the following quantities are introduced: the heat flux ϕ crossing the liquid/solid interface, and $\Delta T = T - T_{s,f}$, the local temperature difference between the average film temperature and the melting temperature of the solid.

$$\begin{aligned} 2\pi r\rho\varepsilon(r)V(r)C_{p,j}\left(T(r)-T_{s,f}\right) &= 2\pi(r+\mathrm{d}r)\rho\varepsilon(r+\mathrm{d}r)V(r+\mathrm{d}r) \\ & \quad C_{p,j}\left(T(r+\mathrm{d}r)-T_{s,f}\right) \\ & \quad +2\pi\phi r\mathrm{d}\mathcal{L} \end{aligned} \tag{21}$$

$$-\frac{\phi}{\cos(\alpha)} = \frac{1}{r}\frac{\mathrm{d}\left(r\rho\varepsilon V C_{p,j}\Delta T\right)}{\mathrm{d}r} \tag{22}$$

Lastly, a jump condition on enthalpy, $\phi = \dot{m}_f\left[L + C_{p,s}\left(T_{s,f} - T_{s,0}\right)\right]$, and Newton's law, here $\phi = h\Delta T$, link equations (20) and (22)[5]. Equation (20) turns into equation (23), while equation (22) turns into equation (24).

$$\frac{StB}{\cos(\alpha)}\theta = \frac{1}{r^*}\frac{\mathrm{d}\left(r^*\varepsilon^* V^*\right)}{\mathrm{d}r^*} \tag{23}$$

[4] *i.e.* the mass of liquid produced by melting per unit area.

[5] $\phi = \dot{m}_f\left[L + C_{p,s}\left(T_{s,f} - T_{s,0}\right)\right]$ is another way of writting equation (9).

$$-\frac{St}{\cos(\alpha)}\theta = \frac{1}{r^*}\frac{\mathrm{d}\left(r^*\varepsilon^* V^*\theta\right)}{\mathrm{d}r^*} \tag{24}$$

Equations (23) & (24) are scaled using the melting number B and the Stanton number $St = \frac{h}{V_j \rho_j C_{p,j}}$, as well as the scaled variables listed in (25).

$$r^* = \frac{r}{D_j}\ ; \quad \varepsilon^* = \frac{\varepsilon}{D_j}\ ; \quad V^* = \frac{V}{V_j}\ ; \quad \theta = \frac{T - T_{s,f}}{T_j - T_{s,f}} \tag{25}$$

Assuming that h is constant requires that the ratio of melting velocities V_f^0/V_f is equal to the ratio $\Delta T_0/\Delta T$, *cf.* equation (10). Therefore, equations (3) & (5) give equation (26), where $z^* = z/D_j$.

$$\cos(\alpha) = \frac{\theta}{\theta_0}\ ; \quad \text{and} \quad \frac{\mathrm{d}z^*}{\mathrm{d}r^*} = \sqrt{\left(\frac{\theta_0}{\theta}\right)^2 - 1}. \tag{26}$$

The effect of gravity can be added considering the momentum balance. The local momentum balance at steady-state writes as equation (27) if shear stress at the liquid/solid interface is neglected.

$$\left[2\pi(r+\mathrm{d}r)\rho\varepsilon(r+\mathrm{d}r)V^2(r+\mathrm{d}r) - 2\pi r\rho\varepsilon(r)V^2(r)\right]\boldsymbol{T} = 2\pi r\rho\varepsilon(r)\boldsymbol{g}\mathrm{d}\mathcal{L} \tag{27}$$

Equation (27) can be projected upon the vertical axis. Noting that $\boldsymbol{T}\cdot\boldsymbol{e_z} = -\sin(\alpha)$, the momentum balance transforms into equation (28) and finally into equation (29) after going to the limit $dr \to 0$ and scaling the terms according to (25). A new well-known dimensionless number appears as being the Froude number $Fr = \frac{V_j}{\sqrt{gD_j}}$.

$$\begin{gathered}\sin(\alpha)\left[\frac{\rho\varepsilon(r+\mathrm{d}r)V^2(r+\mathrm{d}r) - \rho\varepsilon(r)V^2(r)}{\mathrm{d}r} + \frac{\rho\varepsilon(r+\mathrm{d}r)V^2(r+\mathrm{d}r)}{r}\right] \\ = \rho\varepsilon(r)g\frac{\mathrm{d}\mathcal{L}}{\mathrm{d}r}\end{gathered} \tag{28}$$

$$\frac{1}{r^*}\frac{\mathrm{d}\left(r^*\varepsilon^*\left(V^*\right)^2\right)}{\mathrm{d}r^*}\sin(\alpha) = -\frac{\varepsilon^*}{Fr^2}\frac{1}{\cos(\alpha)} \tag{29}$$

Equation (26) can now be used in conjunction with some trigonometry, *i.e.* $\sin(\alpha) = \sqrt{1 - \left(\frac{\theta}{\theta_0}\right)^2}$, to write the set of ordinary differential equations (30) which finally defines the CTH model.

$$\boxed{\begin{cases} \dfrac{\mathrm{d}\left(r^*\varepsilon^*V^*\right)}{\mathrm{d}r^*} = StB\theta_0 \\ \dfrac{1}{r^*}\dfrac{\mathrm{d}\left(r^*\varepsilon^*V^*\theta\right)}{\mathrm{d}r^*} = -St\theta_0 \\ \dfrac{1}{r^*}\dfrac{\mathrm{d}\left(r^*\varepsilon^*\left(V^*\right)^2\right)}{\mathrm{d}r^*}\sqrt{1-\left(\dfrac{\theta}{\theta_0}\right)^2} = -\dfrac{\varepsilon^*}{Fr^2}\dfrac{\theta_0}{\theta} \\ \dfrac{\mathrm{d}z^*}{\mathrm{d}r^*} = \sqrt{\left(\dfrac{\theta_0}{\theta}\right)^2-1} \end{cases}} \tag{30}$$

6. Experimental validation

To assess the validity of the BLG models, equations (15) & (16), and the CTH model, equation (30), they were confronted to experiments performed with HAnSoLO setup [9]. It used water for the liquid jet and transparent ice for the solid. The jet was surrounded with air up to its arrival upon the solid surface. Details on HAnSoLO are available in [22, 23, 9]. In these experiments the jet was turbulent, but became laminar at impact [6]. The main difference between an initially laminar and an initially turbulent jet is the location of the onset of turbulence, which is observed closer to the jet impact point and is less affected by the jet Reynolds number for turbulent jets [26, 11]. The comparisons are done directly on cavity images taken by high speed camera to rule out any bias due to image analysis procedure. The comparisons are done in Figures 6 & 7. In order to maximize the visible portion of the cavity, comparisons are made at the end of the film regime just before the transition toward pool regime. The reader is referred to the supplementary materials for a video comparing the BLG-2 model, equation (16), and the constant h model, equation (30), to an experimental cavity developing in film regime. The experiment used in the video corresponds to the one in Figures 6b & 7b.

[6] It has been shown in [9].

	Figure 6			Figure 7		
	a	b	c	a	b	c
D_j $[mm]$	5	5.9	9.4	5	5.9	6.0
T_j $[^oC]$	30	50	31	30	50	71
V_j $\left[m.s^{-1}\right]$	1.5	5.1	2.8	1.5	5.1	10.1
h $\left[kW.m^{-2}.K^{-1}\right]$	-			12	19	38
Re $[-] \times 10^3$	11	55	35	11	55	147
Pr $[-]$	5.4	3.6	5.3	5.4	3.6	2.5
St $[-] \times 10^{-3}$	2.0	0.9	1.1	2.0	0.9	0.9
B $[-]$	0.37	0.63	0.38	0.37	0.63	0.88
Fr $[-]$	-			6.7	21.2	41.5

Table 1: Relevant physical parameters for experiments reported in Figures 6 & 7. Figures 6b and 7b are from the same experiment.

6.1. Boundary layer growth models

Photographs of the cavity recorded from three experiments are compared to the BLG models defined by equations sets (15) & (16) in Figure 6. Important parameters are reported for each experiment in Table 1. These experiments represent the different situations which can be encountered when the boundary layer growth zone is visible, *cf.* Figure 2a. FIn Figure 6, (a) is representative of the case for which the boundary layer zone makes up for almost all the visible cavity, (b) shows a typical case where both a boundary layer zone and a turbulent zone are visible, (c) is identical to the second one but was obtained with a larger jet diameter. The results of both BLG models (with, or without curvature) are close to each other and to the cavity in the boundary layer zone. However, the model taking the curvature into account (BLG-2) matches the experimental visualizations more closely. These models can therefore be used to assess the cavity shape when only the boundary layer zone is expected. Also as the BLG model underestimates the cavity volume outside the boundary layer

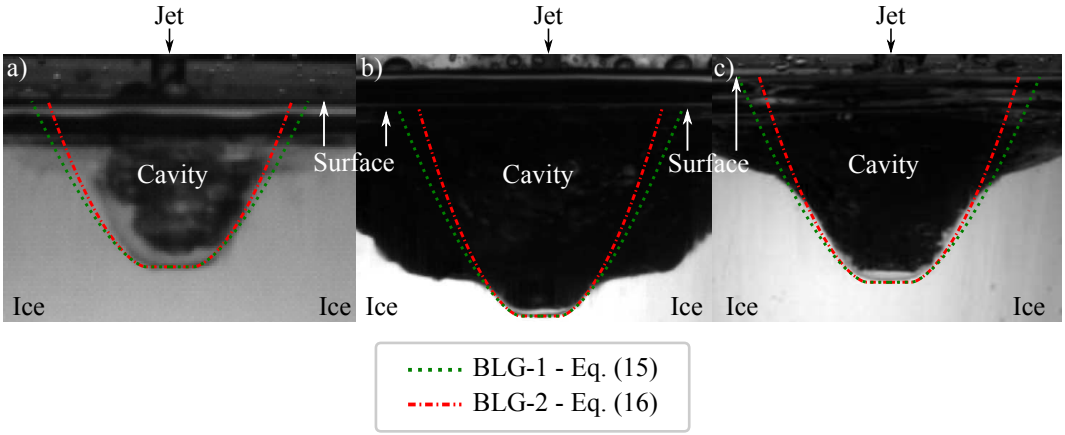

Figure 6: Experimental visualization of cavity shapes presented alongside numerical predictions computed using BLG models (BLG-1: equations (15) & BLG-2: equations (16)). The full video for (b) is available in supplementary materials. Relevant physical parameters are reported in Table 1.

growth zone can give a lower estimate for the cavity volume.

6.2. Constant h model

Photographs of the cavity recorded from three representative experiments are confronted to the CTH model defined by equations set (30) in Figure 7. Important parameters are reported for each experiment in Table 1. Experiments represented in Figures 7a&b are the same as in Figure 6a&b in order to compare the BLG models to the CTH model. The experiment represented in Figure 7c corresponds to a case for which the boundary layer zone is not visible, *cf.* Figure 2a. The values of h used for the computations is reported in Table 1. These values of h were determined in [9] from ablation velocity data by using equation (2).

The cavity shapes predicted by the CTH model are wider than the ones computed with the BLG models. For the experiments where the boundary layer zone is visible, the constant h model describes the global shape of the cavity outside of the boundary layer zone well. When the boundary layer zone is not visible, the CTH model gives an operational estimate, in order of magnitude,

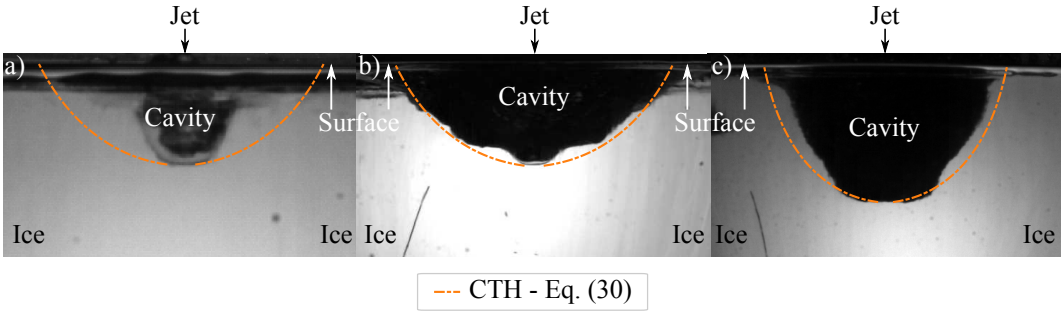

Figure 7: Experimental visualization of cavity shapes with an overlay of the cavity shapes predicted using CTH model – equations (30). The full video of (b) is available in supplementary materials. Relevant physical parameters are reported in Table 1.

of the global shape of the cavity, *cf.* Figure 7c. The actual cavity is mostly confined within the limits given by the model. Therefore, it can provide an upper limit for the cavity volume. As the BLG models give a lower limit, this yields an interval of cavity volume which covers the real cavities. The models presented here can be used to design structures that must withstand ablation by a liquid jet, like core-catcher reinforcement pods in nuclear designs.

The CTH model can also be used to obtain the temperature of the liquid film at a given distance from impact. An example of such a computation is given in Figure 8. The computed data are compared with infrared measurements of the liquid film surface temperature from [12]. The values predicted with CTH model follow the experimental values up to $r^* \approx 7.5$.

One limitation of both BLG and CTH models is that they are only valid until transition to pool regime which can however be estimated using the model described in [12].

7. Conclusion

A mathematical model linking the local cavity shape, described by the local angle of the liquid/solid interface, to the ratio of the local melting velocity over the melting velocity at impact is presented. Two modeling approaches are considered for the local melting velocity. The first approach (BLG models)

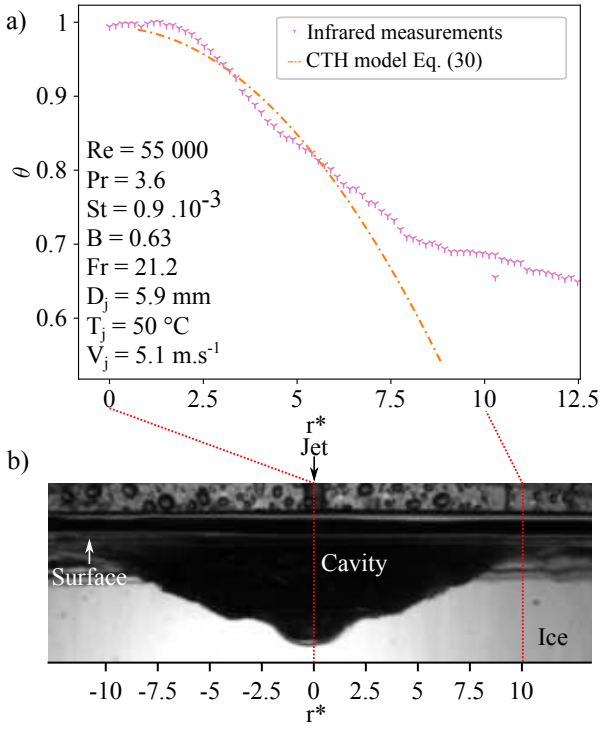

Figure 8: (a) Evolution of θ at the gas/liquid interface measured by infrared camera compared with the results computed with the CTH model – equations (30). (b) Cavity shape at time of infrared measurement. This experiment is the same as in Figures 6b and 7b.

assumes that temperature in the liquid film is constant while the heat transfer resistance increases with the radial distance from impact, *i.e.* the heat transfer coefficient h decreases. This assumption is considered representative of the boundary layer growth zone, *cf.* Figure 2a. The second approach (CTH model) assumes that the heat transfer resistance remains constant, *i.e.* h is constant, while the film temperature decreases with the radial distance from impact. This assumption is considered representative of cavities for which the boundary layer growth zone is not visible, *cf.* Figure 2b. For such cavity type the liquid film is mostly turbulent. It led to two types of models referred to as BLG and CTH models.

The predictions from the boundary layer growth models (BLG) and the constant h model (CTH) are compared with experimental data acquired from HAnSoLO experimental setup [9]. The BLG models describe the cavity shape in the boundary layer growth zone well, but are not valid outside. The CTH model gives a global shape coherent with the experimental cavity shape in the turbulent zone. Liquid film temperature evolution obtained using the CTH model is consistent with the experimental data for $r^* \lesssim 7.5$.

The actual cavity is mostly confined within the limits given by the two models (BLG and CTH). Therefore, these two models can provide a lower and an upper bound for the cavity volume. This can be seen in the supplementary video.

The presented models can help for design of solid devices which must withstand ablation by a hot liquid jet, like for instance the core-catcher of future SFR.

8. Acknowledgments

The research carried in the frame of the ESFR-SMART project leading to some part of results has received funding from the Euratom research and training program 2014-2018 under grant agreement N° 754501.

We thank Michael Johnson for English proof reading.

9. Declaration of Interests

The authors report no conflict of interest.

References

[1] F. Bertrand, N. Marie, A. Bachrata, V. Brun-Magaud, J. Droin, X. Manchon, K. Herbreteau, B. Farges, B. Carluec, S. Poumerouly, D. Lemasson, Status of severe accident studies at the end of the conceptual design of ASTRID: Feedback on mitigation features, Nucl. Eng. Des. 326 (2018) 55 – 64. doi:10.1016/j.nucengdes.2017.10.019.

[2] IRSN, Research and development with regard to severe accidents in pressurised water reactors: Summary and outlook, Tech. Rep. IRSN-2007/83, IRSN (2007).
URL https://www.irsn.fr/FR/Larecherche/publications-documentation/Publications_documentation/BDD_publi/DSR/SAGR/Documents/rapport_RetD_AG_VA.pdf

[3] G. Albrecht, F. Huber, E. Jenes, A. Kaiser, W. Schütz, KAJET experiments on pressure-driven melt jets and their interaction with concrete, Tech. Rep. FZKA-7002, KIT (2005). doi:10.5445/IR/270060425.

[4] Reactor Harmonization Group RHWG, Safety of new NPP designs, Tech. rep., Western European Nuclear Regulators Association (Mar. 2013).

URL http://www.wenra.org/media/filer_public/2013/08/23/rhwg_safety_of_new_npp_designs.pdf

[5] F. Gauché, Generation IV reactors and the ASTRID prototype: Lessons from the fukushima accident, C. R. Phys. 13 (4) (2012) 365 – 371. doi:10.1016/j.crhy.2012.03.004.

[6] F. Payot, C. Journeau, C. Suteau, F. Serre, M. Gradeck, N. Rimbert, A. Lecoanet, A. Miassoedov, A new experimental R&D program associated with the corium jet impingement on the ASTRID core catcher sacrificial material, in: Proc. of ICAPP 2018, ANS, Charlotte, NC, USA, 2018, pp. 657–666. doi:10.5281/zenodo.1309374.

[7] J. Guidez, A. Gerschenfel, J. Bodi, K. Mikityuk, F. Alvarez-Velarde, P. Romojaro, U. Diaz-Chiron, ESFR SMART project conceptual design of in-vessel core catcher, EPJ Web Conf. 247 (2021) 01002. doi:10.1051/epjconf/202124701002.

[8] R. Le Tellier, Mass transfer induced rayleigh-taylor instabilities between two immiscible liquids: The unique case of corium, in: Proceedings of the 9th International Conference on Fluid Flow, Heat and Mass Transfer (FFHMT'22), Niagara Falls, Canada, 2022, pp. 148–1–148–8. doi:10.11159/ffhmt22.148.

[9] A. Lecoanet, F. Payot, C. Journeau, N. Rimbert, M. Gradeck, Study of the ablation consecutive to jet impingement on a meltable solid – Application to SFR core-catcher, Nucl. Eng. Des. 377 (2021) 111147. doi:10.1016/j.nucengdes.2021.111147.

[10] M. Saito, K. Sato, A. Furutani, M. Isozaki, S. Imahori, Y. Hattori, Melting attack of solid plates by a high temperature liquid jet — effect of crust formation, Nucl. Eng. Des. 121 (1) (1990) 11 – 23. doi:10.1016/0029-5493(90)90003-G.

[11] H. J. V. Lienhard, Annual review of heat transfer, in: C.-L. Tien (Ed.), Annual Review of heat transfer, Vol. 6, Begell house inc., New York, Wallingford (U.K.), 1995, Ch. Liquid jet impingement, pp. 199 – 270. doi:10.1615/AnnualRevHeatTransfer.v6.60.

[12] A. Lecoanet, F. Payot, C. Journeau, N. Rimbert, M. Gradeck, Classification of ablation mode during impact of hot liquid jet on a solid, Int. J. Heat Mass Transf. 181 (2021) 121883. doi:10.1016/j.ijheatmasstransfer.2021.121883.
URL https://hal.univ-lorraine.fr/hal-03341319

[13] L. Roberts, On the melting of a semi-infinite body of ice placed in a hot stream of air, J. Fluid Mech. 4 (5) (1958) 505–528. doi:10.1017/S002211205800063X.

[14] M. J. Swedish, M. Epstein, J. H. Linehan, G. A. Lambert, G. M. Hauser, L. J. Stachyra, Surface ablation in the impingement region of a liquid jet, AIChE J. 25 (4) (1979) 630–638. doi:10.1002/aic.690250409.

[15] M. Esptein, The effect of melting on heat transfer to submerged bodies, Lett. Heat Mass Transf. 2 (2) (1975) 97 – 103. doi:10.1016/0094-4548(75)90047-8.

[16] O. M. Griffin, Heat, mass, and momentum transfer during the melting of glacial ice in sea water, J. Heat Transfer 95 (3) (1973) 317–323. doi:10.1115/1.3450058.

[17] A. Furutani, S. Imahori, K. Sato, M. Saito, Erosion behavior of a solid plate by a liquid jet - effect of molten layer, Nucl. Eng. Des. 132 (2) (1991) 153 – 169. doi:10.1016/0029-5493(91)90263-H.

[18] D. A. Powers, Erosion of steel structures by high-temperature melts, Nucl. Sci. Eng. 88 (3) (1984) 357–366. arXiv:https://doi.org/10.13182/NSE84-A18589, doi:10.13182/NSE84-A18589.
URL https://doi.org/10.13182/NSE84-A18589

[19] K. Sato, A. Furutani, M. Saito, M. Isozaki, K. Suganuma, S. Imahori, Melting attack of solid plates by a high-temperature liquid jet [II] — erosion behavior by a molten metal jet, Nucl. Eng. Des. 132 (2) (1991) 171 – 186. doi:10.1016/0029-5493(91)90264-I.

[20] H. Schlichting, J. Kestin, Boundary-layer theory [Texte imprimé], McGraw-Hill series in mechanical engineering, New York : McGraw-Hill. cop. 1979., 1979.

[21] A. Lipsett, R. R. Gilpin, Laminar jet impingement heat transfer including the effects of melting, Int. J. Heat Mass Transf. 21 (1978) 25 – 33. doi:10.1016/0017-9310(78)90152-7.

[22] A. Lecoanet, N. Rimbert, M. Gradeck, F. Payot, Ablation d'un bloc de glace transparente par un jet d'eau chaude – Application à la sûreté des RNR-Na, Entropie 1 (4) (2020). doi:10.21494/ISTE.OP.2020.0519.

[23] A. Lecoanet, Étude de l'ablation d'une paroi solide par un jet liquide, Ph.D. thesis, Université de Lorraine (2021).
URL http://www.theses.fr/2021LORR0015

[24] A. Lecoanet, M. Gradeck, X. Gaus-Liu, T. Cron, B. Fluhrer, F. Payot, C. Journeau, N. Rimbert, Ablation of a solid material by high temperature liquid jet impingement: an application to corium jet impingement on a SFR core-catcher, ASME J. of Nuclear Rad. Sci. (2021). doi:10.1115/1.4051448.

[25] W. Tromm, X. Gaus-Liu, KIT-JIMEC experiments to investigate jet impingement on the ablation of core catcher bottom, in: 30th International Conference Nuclear Energy for New Europe (NENE30), Bled, Slovenia, 2021.

[26] J. Stevens, B. W. Webb, Local heat transfer coefficients under an axisymmetric, single-phase liquid jet, J. Heat Transfer 113 (1) (1991) 71–78. doi:10.1115/1.2910554.